


Temperature-Dependent Studies of Coupled Fe₅₅Pt₄₅/Fe₄₉Rh₅₁ Thin Films

R. A. Griffiths, J. L. Warren, C. W. Barton, J. J. Miles, P. W. Nutter,* and T. Thomson
Nano Engineering & Storage Technologies Research Group, School of Computer Science, The University of Manchester, Oxford Road, Manchester, M13 9PL, UK

 (Received 25 April 2018; revised manuscript received 9 July 2018; published 7 November 2018)

Equiatomic Fe₅₀Rh₅₀, with its highly unusual antiferromagnetic to ferromagnetic phase transition at approximately 370 K, provides the ability to create artificial multifunctional materials when combined with high-anisotropy magnetic thin films in an exchange-mediated structure. We investigate the temperature dependence of switching in L₁₀ Fe₅₅Pt₄₅/Fe₄₉Rh₅₁ bilayer thin films, where the Fe₄₉Rh₅₁ assists the switching of the Fe₅₅Pt₄₅ at modestly increased temperatures. A simple layered macrospin model is able to capture the switching characteristics of these films and shows good agreement with experimental results. Patterned L₁₀ Fe₅₅Pt₄₅/Fe₄₉Rh₅₁ structures, measured using the anomalous Hall effect, show a similar temperature-dependent switching behavior, paving the way for reduced switching fields in future applications including heat-assisted bit-patterned-media recording and spintronic devices.

DOI: [10.1103/PhysRevApplied.10.054015](https://doi.org/10.1103/PhysRevApplied.10.054015)

I. INTRODUCTION

Fe₅₀Rh₅₀ is a highly unusual alloy that exhibits a first-order meta-magnetic phase transition, from antiferromagnetic (AFM) to ferromagnetic (FM) at temperatures above room temperature (greater than approximately 370 K) over a narrow range of compositions (Fe content from approximately 48 to 54 at. %) [1,2]. This phase transition is accompanied by a change in lattice constant of 0.3% and a large reduction (approximately 60%) in electrical resistance [3–6]. These properties make it an attractive material for applications including heat-assisted magnetic recording [5–8], spintronics [9,10], antiferromagnetic memory resistors [11], and hyperthermia treatments [12]. Engineering interfacial-exchange interactions where magnetically ordered thin films are placed in intimate proximity allows new, multi-functional materials to be created. In particular, combining high-perpendicular anisotropy FM films such as ordered L₁₀ Fe₅₀Pt₅₀ [5] with Fe₅₀Rh₅₀ results in a system where the field required to switch the film can be reduced through moderate heating [13,14]. A potential reduction in the switching field of up to 75% can be achieved using this approach, leading to fast switching at lower energy cost compared with Curie point switching [15,16]. In addition, since Fe₄₉Rh₅₁ is antiferromagnetic at room temperature, the thermal

stability of Fe₅₅Pt₄₅ can be enhanced through exchange bias. Subsequent patterning of these material systems into nanostructures, for applications such as heat-assisted bit-patterned-media recording [17,18], offers the promise of significant increases in areal density while still maintaining the necessary thermal stability.

Here, we investigate the temperature-dependent switching of Fe₅₅Pt₄₅/Fe₄₉Rh₅₁ bilayer thin films where the Fe₅₅Pt₄₅ layer is in the L₁₀ phase with perpendicular anisotropy and the Fe₄₉Rh₅₁ layer is in the B2 phase that exhibits the AFM to FM phase transition. The magnetic properties of the films as a function of temperature are characterized using vector vibrating sample magnetometry (V VSM). We also pattern structures from these films and the temperature-dependent switching of meso-scale islands is investigated using the anomalous Hall effect (AHE), which offers the high sensitivity required to observe the switching of individual, isolated magnetic elements [19].

A layered macrospin model has been developed to simulate the switching process in these exchange-mediated bilayers. The model has been used to simulate hysteresis loops as a function of temperature allowing direct comparison with experimental data. Optimizing the model parameters to match the data allows good estimates of the material parameters, such as exchange constants, to be made.

II. THIN-FILM FABRICATION AND CHARACTERIZATION

An Fe₅₅Pt₄₅(11)/Fe₄₉Rh₅₁(30)/Pt(2) (dimensions in nm, composition in at. %) thin film is deposited on to MgO(100) substrates using dc-magnetron sputtering; full details of the thin-film fabrication process are

*p.nutter@manchester.ac.uk

Published by the American Physical Society under the terms of the *Creative Commons Attribution 4.0 International license*. Further distribution of this work must maintain attribution to the author(s) and the published article's title, journal citation, and DOI.

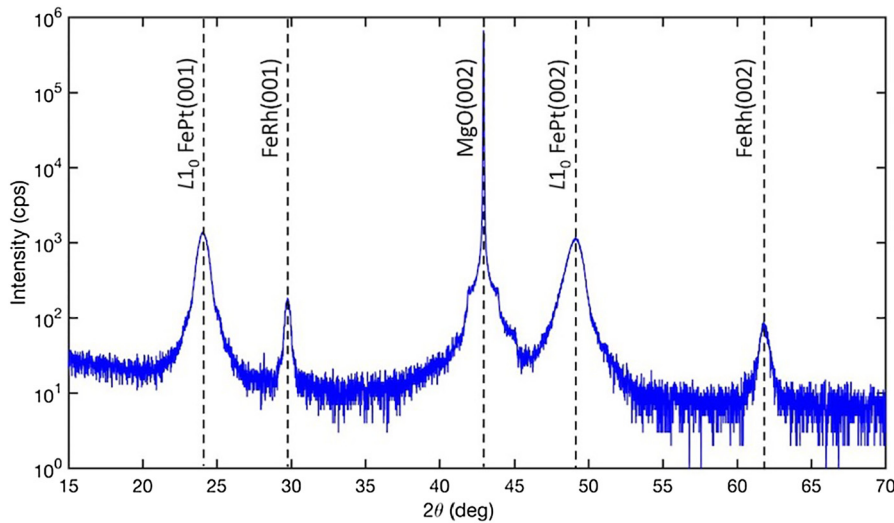


FIG. 1. XRD spectra (θ - 2θ geometry) for the as-deposited $\text{Fe}_{55}\text{Pt}_{45}/\text{Fe}_{49}\text{Rh}_{51}$ thin film showing the characteristic analysis peaks (labeled).

presented in the Appendix. X-ray diffraction (XRD) measurements of the as-deposited thin film (θ - 2θ geometry) are performed at room temperature using a Rigaku SmartLab Diffractometer fitted with a Ge(220) two-bounce monochromator. Figure 1 shows the XRD spectra and characteristic peaks for the fabricated $\text{Fe}_{55}\text{Pt}_{45}/\text{Fe}_{49}\text{Rh}_{51}$ film.

The presence of the $\text{Fe}_{55}\text{Pt}_{45}$ superlattice (001) and $\text{Fe}_{55}\text{Pt}_{45}$ fundamental (002) peaks indicate that a highly ordered $L1_0$ (face-centered-tetragonal unit cell) film is produced. The order parameter, S , can be calculated using

$$S \approx 0.497 \left(\frac{I_{001}}{I_{002}} \right)^{1/2}, \quad (1)$$

where I_{001} and I_{002} are the integrated intensities of the $\text{Fe}_{55}\text{Pt}_{45}$ (001) and (002) peaks, respectively [20]. To determine values for the integrated intensities, I_{001} and I_{002} , values are taken from the Rigaku GlobalFit software using the XRD data in Fig. 1. Using the methodology presented in Ref. [20], we calculate the $\text{Fe}_{55}\text{Pt}_{45}$ order parameter, S , to be 0.55, which is consistent with previously published work [20,21], where the order parameter of segregated granular $\text{Fe}_{55}\text{Pt}_{45}$ films is shown to be in the range 0.38–0.91. The order parameter is sufficient to ensure good perpendicular anisotropy while allowing switching using moderate applied fields. The presence of the $\text{Fe}_{49}\text{Rh}_{51}$ superlattice (001) and fundamental (002) peaks demonstrate that the $\text{Fe}_{49}\text{Rh}_{51}$ layer is (001) orientated and that the required B2 (bcc unit cell) crystal structure is achieved [14,15].

Room temperature (22 °C) in-plane (longitudinal) and out-of-plane (perpendicular) hysteresis loops are produced for the fabricated $\text{Fe}_{55}\text{Pt}_{45}/\text{Fe}_{49}\text{Rh}_{51}$ bilayer thin film using a MicroSense Model 10 V VSM, as shown in Fig. 2, where the out-of-plane and in-plane moments have been normalized with respect to the $\text{Fe}_{55}\text{Pt}_{45}$ and $\text{Fe}_{49}\text{Rh}_{51}$ layer volumes, respectively. The out-of-plane loop has

a squareness of 0.762 with a coercivity of 4.6 kOe, indicating a well-oriented film with good perpendicular anisotropy. The out-of-plane saturation moment, M_s , of the film (approximately 1500 emu/cm³) includes contributions from both the $\text{Fe}_{55}\text{Pt}_{45}$ and $\text{Fe}_{49}\text{Rh}_{51}$ layers.

To determine the temperature dependence of the bilayer film, the in-plane and out-of-plane moments are measured as a function of temperature, as shown in Fig. 3. A constant in-plane field of 1 kOe is applied to ensure saturation of any in-plane magnetic moment and the film is saturated out-of-plane prior to each measurement to ensure the $\text{Fe}_{55}\text{Pt}_{45}$ layer is aligned out-of-plane. As no perpendicular field is applied during the measurement, the out-of-plane moment does not include any contribution arising from the $\text{Fe}_{49}\text{Rh}_{51}$ layer. Evidence of an in-plane (non-zero) moment at room temperature demonstrates the $\text{Fe}_{49}\text{Rh}_{51}$ has a FM component at room temperature, as corroborated by the in-plane hysteresis loop in Fig. 2. The

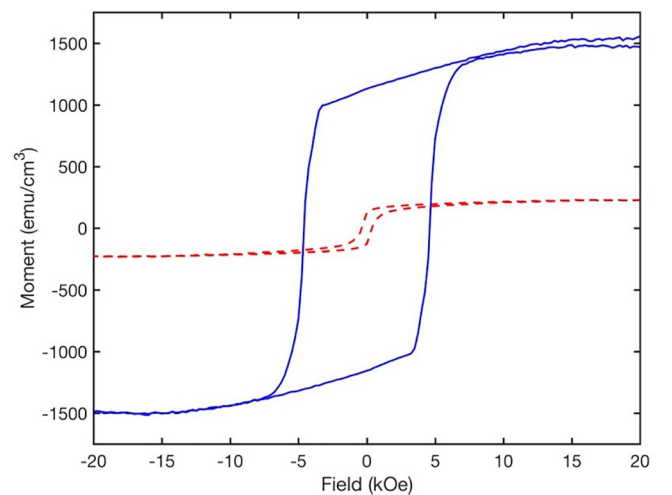


FIG. 2. In-plane (red, dashed line) and out-of-plane (blue, solid line) hysteresis loops of the $\text{Fe}_{55}\text{Pt}_{45}/\text{Fe}_{49}\text{Rh}_{51}$ bilayer thin film measured by V VSM at room temperature (22°).

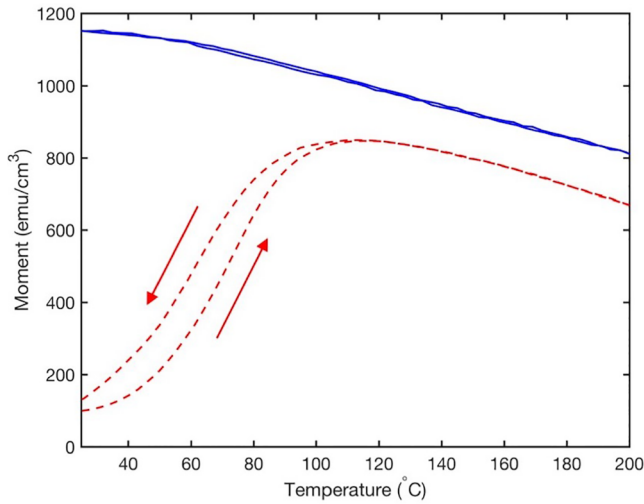


FIG. 3. Measured in-plane (red, dashed line) and out-of-plane (blue, solid line) moments (emu/cm^3) as a function of temperature, measured under a constant in-plane field of 1 kOe. The film is saturated out-of-plane prior to each measurement.

in-plane moment shows the characteristic thermal hysteresis due to the presence of the AFM to FM transition in the $\text{Fe}_{49}\text{Rh}_{51}$ [22]. The peak moment for the in-plane signal is $847 \text{ emu}/\text{cm}^3$, which occurs as the AFM to FM transition is completing at approximately 110°C , which is far from the Curie temperature for the $\text{Fe}_{55}\text{Pt}_{45}$ film (in excess of 450°C [23]). This moment is slightly lower than reported values of $\text{Fe}_{49}\text{Rh}_{51}$, for example, Thiele *et al.* [13] gave a figure of $1270 \text{ emu}/\text{cm}^3$ for a 60-nm $\text{Fe}_{49}\text{Rh}_{51}$ film. However, our measured peak moment is consistent with results published by Barton *et al.* of approximately $860 \text{ emu}/\text{cm}^3$ for a 10-nm film [24]. These values are characteristic of a well-defined interface between the $\text{Fe}_{55}\text{Pt}_{45}$ and $\text{Fe}_{49}\text{Rh}_{51}$ layers. However, the exact nature of the structural interface is not determined as part of this work.

The temperature dependence of the $\text{Fe}_{55}\text{Pt}_{45}$ moment can be seen in the out-of-plane signal, which gradually decreases with temperature according to the standard Weiss theory [25], with the peak moment of $1151 \text{ emu}/\text{cm}^3$ at room temperature consistent with the expected value of $1140 \text{ emu}/\text{cm}^3$ found in bulk $\text{Fe}_{55}\text{Pt}_{45}$ [26]. The slight increase in the $\text{Fe}_{55}\text{Pt}_{45}$ moment along with a reduced $\text{Fe}_{49}\text{Rh}_{51}$ moment can be explained by the moment of the $\text{Fe}_{49}\text{Rh}_{51}$ at the $\text{Fe}_{55}\text{Pt}_{45}/\text{Fe}_{49}\text{Rh}_{51}$ interface being held out-of-plane due to exchange coupling with the $\text{Fe}_{55}\text{Pt}_{45}$, within the exchange length estimated to be 12 nm [13].

Figure 4 shows a series of out-of-plane hysteresis loops measured by V VSM at a range of temperatures from room temperature to 200°C . In each case, the temperature is allowed to stabilize before the measurement is taken and the moment is normalized by the total film volume (8-mm-diameter sample, $20 \times 10^{-7} \text{ cm}^3$ volume). As the temperature is increased, the moment can be seen to rise

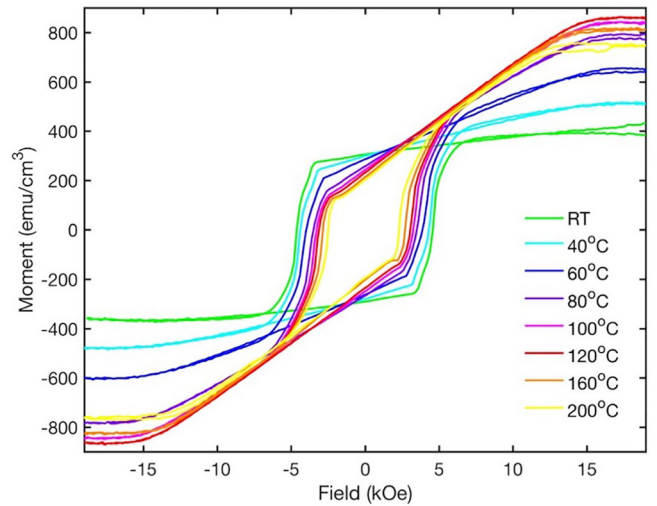


FIG. 4. Out-of-plane hysteresis loops produced using the V VSM for a range of temperatures from room temperature (RT = 22°C) through the transition temperature of the $\text{Fe}_{49}\text{Rh}_{51}$ layer up to a final temperature of 200°C .

at an almost linear rate as the field is increased, leading to a temperature dependence in M_s . To analyze the dependency on temperature, values of coercivity, H_c , and M_s are extracted from the hysteresis loops in Fig. 4 and are plotted in Fig. 5 as a function of temperature.

The increase in M_s up to 120°C and subsequent reduction for higher temperatures follows the temperature dependency of the in-plane $\text{Fe}_{49}\text{Rh}_{51}$ FM component, which is pulled out-of-plane for higher applied fields. Key

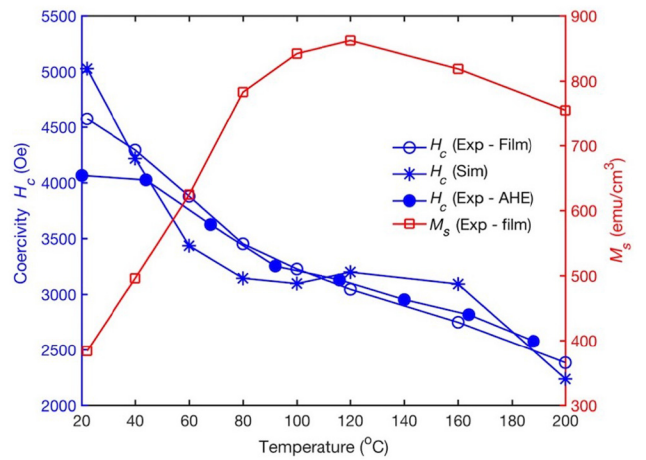


FIG. 5. Temperature dependence of coercivity, H_c , (open blue circles) and saturation moment, M_s , (open red squares) for the $\text{Fe}_{55}\text{Pt}_{45}/\text{Fe}_{49}\text{Rh}_{51}$ bilayer extracted from the experimental hysteresis loops in Fig. 4. Also shown is the temperature variation of H_c (blue stars) using the macrospin model presented in Sec. III, which is extracted from the simulated hysteresis loops in Fig. 6, and the temperature dependence of coercivity for the patterned island (closed blue circles) measured using AHE.

to the practical applications of this material system is that the coercivity reduces with temperature, decreasing more sharply over the temperature interval where the FM phase of Fe₄₉Rh₅₁ develops (approximately 40–100 °C). This decrease in coercivity is in excess of that expected due to temperature changes alone [27] suggesting that the developing FM phase in the Fe₄₉Rh₅₁ layer is assisting the switching of the Fe₅₅Pt₄₅ via an exchange-spring mechanism.

III. MACROSPIN MODEL

In order to understand the magnetization processes within the Fe₅₅Pt₄₅/Fe₄₉Rh₅₁ bilayer, a simple model is adopted that treats the system as macrospins, splitting the Fe₅₅Pt₄₅ and Fe₄₉Rh₅₁ layers into lateral sublayers, with each material being represented as a number of sublayers stacked vertically with each sublayer represented as a single spin. The 11-nm-thick Fe₅₅Pt₄₅ layer is treated as two 5.5-nm-thick sublayers and the 30-nm-thick Fe₄₉Rh₅₁ layer is treated as six 5-nm-thick sublayers, yielding eight sublayers in total. While the model cannot capture any in-plane variations of moment, the differing vertical interactions between the sublayers are described and the model allows vertical variation of the moment with some smoothing of magnetization transitions around the Fe₅₅Pt₄₅/Fe₄₉Rh₅₁ boundary.

The model treats each of the sublayers as a single macrospin that obeys the well-known Landau–Lifshitz equation in the Gilbert form (LLG):

$$\frac{d\vec{M}_i}{dt} = \frac{-\gamma}{1+\alpha^2}(\vec{M}_i \times \vec{H}_i) - \frac{\alpha\gamma}{1+\alpha^2} \frac{\vec{M}_i \times (\vec{M}_i \times \vec{H}_i)}{|\vec{M}_i|} \quad (2)$$

where

$$\frac{\gamma}{1+\alpha^2} = \gamma_L < 0 \quad (3)$$

is the Landau–Lifshitz electron gyromagnetic ratio (the ratio of the magnetic dipole moment to the angular momentum of the system), α is a phenomenological damping constant, and i denotes a specific sublayer.

In the simulations, we compute hysteresis loops that can then be compared with the experimental out-of-plane hysteresis loops. However, it is not computationally feasible to integrate the LLG equation over time scales of minutes, so we calculate hysteresis loops with half-loop times of 50 ns and $\alpha = 1$, which acts to minimize the impact of precession on the simulated loops allowing comparison with the long timescale experimental loops [28].

In the model, the effective field, H_i , in (2) includes the externally applied field H_E , an anisotropy field H_A , a shape-demagnetizing field for each sublayer H_S , a magnetostatic-interaction field accounting for the magnetostatic field from all other sublayers H_M , and an exchange field that accounts for the vertical exchange

interaction between sublayers H_X . The model does not include stochastic thermal effects. Deterministic thermal effects, such as variation in M_s , anisotropy, and exchange are accommodated by varying the values of the parameters according to appropriate functions of temperature.

The experimentally measured samples have a diameter of 8 mm and each sublayer is around 5-nm thick so the diameter:thickness ratio is greater than 10^6 . This allows the sublayers to be treated as effectively having infinite lateral dimensions, giving a shape-demagnetizing field equal to that of an infinite sheet [in centimeter-gram-second (cgs) units]:

$$\vec{H}_{Si} = 4\pi M_{zi} \hat{z} \quad (4)$$

where the z direction is perpendicular to the plane. The magnetostatic-interaction field between vertically stacked infinite sheets is zero and so is not included in the simulations. The anisotropy of Fe₅₅Pt₄₅ is assumed to be uniaxial perpendicular to the plane and that of Fe₄₉Rh₅₁ is assumed to be uniaxial in-plane, the specific in-plane orientation of the easy axis being unimportant in circular samples.

The exchange field experienced by sublayer i due to the magnetization of an adjacent sublayer j is calculated using a dimensionless exchange parameter C :

$$\vec{H}_{Xi} = C_{ij} 4\pi \vec{M}_j \quad (5)$$

where C_{ij} may differ according to the compositions of layers i and j . In the Fe₅₅Pt₄₅/Fe₄₉Rh₅₁ system, there are three exchange constants: C_1 , C_2 , and C_3 , representing the exchange coupling between Fe₅₅Pt₄₅/Fe₅₅Pt₄₅, Fe₅₅Pt₄₅/Fe₄₉Rh₅₁ and Fe₄₉Rh₅₁/Fe₄₉Rh₅₁ pairs of sublayers, respectively.

The energy per unit volume in sublayer i deriving from the FM exchange with layer j is

$$E_i = -\vec{H}_{Xi} \cdot 4\pi \vec{M}_i = -4\pi C_{ij} \vec{M}_j \cdot \vec{M}_i \quad (6)$$

The exchange interaction energy per unit volume between two layers can also be expressed in terms of the conventional exchange stiffness constant A as

$$E_i = \left(-2A_{ij}/M_s^2 d_{ij}^2 \right) \vec{M}_j \cdot \vec{M}_i, \quad (7)$$

where d_{ij} is the separation between the centers of the layers. It follows that

$$2A_{ij}(T)/M_{si}(T)M_{sj}(T)d_{ij}^2 = 4\pi C_{ij}(T). \quad (8)$$

The relationship between the exchange stiffness constant A and the phenomenological constant C is

$$A_{ij}(T) = [4\pi C_{ij}(T)M_{si}(T)M_{sj}(T)d_{ij}^2]/2. \quad (9)$$

The experimental measurements provide values of $M_s(T)$ for Fe₅₅Pt₄₅ and Fe₄₉Rh₅₁ at different temperatures (Fig. 5)

and these values are used in the model. The out-of-plane experimental loops show two major features: a square switching loop, as would be observed in a high coercivity material with perpendicular anisotropy, and a linear approach to saturation such as would be observed in a material with in-plane anisotropy. While the switching field will be determined by a combination of phenomena, we assume that the saturation field is the point at which the in-plane $\text{Fe}_{49}\text{Rh}_{51}$ layer is brought to a perpendicular orientation by the applied out-of-plane field, at which point the $\text{Fe}_{55}\text{Pt}_{45}$ layer will have already switched. Since we know $M_s(T)$ for $\text{Fe}_{55}\text{Pt}_{45}$ and $\text{Fe}_{49}\text{Rh}_{51}$, we can determine H_K for the $\text{Fe}_{49}\text{Rh}_{51}$ layer by considering the field experienced at the point of saturation, which is the sum of the applied field, the self-demagnetizing field, and the exchange coupling from the $\text{Fe}_{55}\text{Pt}_{45}$, i.e.,

$$H_{K\text{Fe}_{49}\text{Rh}_{51}}(T) = H_{\text{HSat}}(T) - 4\pi M_{s\text{Fe}_{49}\text{Rh}_{51}}(T) + C_2(T) \times 4\pi M_{s\text{Fe}_{55}\text{Pt}_{45}}(T), \quad (10)$$

from which we can calculate the anisotropy constant,

$$K_{1\text{Fe}_{49}\text{Rh}_{51}}(T) = 0.5 \times H_{K\text{Fe}_{49}\text{Rh}_{51}}(T) \times 4\pi M_{s\text{Fe}_{49}\text{Rh}_{51}}(T). \quad (11)$$

The values of the magnetocrystalline anisotropy constant K_1 of $\text{Fe}_{55}\text{Pt}_{45}$, the exchange constants, and Curie temperatures T_C for the $\text{Fe}_{55}\text{Pt}_{45}$ and $\text{Fe}_{49}\text{Rh}_{51}$ thin films are only approximately known, while the form of temperature dependences for the anisotropy constant and the exchange constants are unknown. The temperature dependence of all these parameters is assumed to be of the form

$$X(T) = X(0) \left(1 - \frac{T}{T_C}\right)^x, \quad (12)$$

where x is the exponent for parameter X .

The experimental values of $M_s(T)$ for $\text{Fe}_{55}\text{Pt}_{45}$ are least-squares fitted to (12), with the best fit being obtained for $M_s(0) = 54 \times 10^3 \text{ emu/cm}^3$, $T_C = 314 \text{ }^\circ\text{C}$, and $x_M = 0.396$. The fitted value of x_M is in reasonable agreement with the value of 0.34 obtained by [29]. The value of $M_s(0)$ is greater than while T_C is lower than the literature values of around $1.15 \times 10^3 \text{ emu/cm}^3$ and approximately $430 \text{ }^\circ\text{C}$ [27], respectively. This may be because the experiments are conducted over a relatively narrow temperature range such that although these values fit the experimental measurements of $M_s(T)$ to (12) well within the range $22\text{--}200 \text{ }^\circ\text{C}$, measurements over a more extended range will provide different extrapolated values for M_s and T_C . In terms of the model, the functional form and fitted parameters provide a good description of the measured data over the temperature range of interest.

Initial values are selected for the unknown parameters and their exponents in (10) based on reasonable estimates

TABLE I. Parameter values obtained from the macrospin model.

Parameter	Value
$K_1(0)_{\text{Fe}_{55}\text{Pt}_{45}}$ (perpendicular to the film plane)	$1.77 \times 10^7 \text{ erg/cm}^3$
Power law x for $K_1(T)_{\text{Fe}_{55}\text{Pt}_{45}}$	0.64
$C_1(0)$ $\text{Fe}_{55}\text{Pt}_{45}$ – $\text{Fe}_{55}\text{Pt}_{45}$ exchange constant (dimensionless)	0.4
$C_2(0)$ $\text{Fe}_{55}\text{Pt}_{45}$ – $\text{Fe}_{49}\text{Rh}_{51}$ exchange constant (dimensionless)	0.31
$C_3(0)$ $\text{Fe}_{49}\text{Rh}_{51}$ – $\text{Fe}_{49}\text{Rh}_{51}$ exchange constant (dimensionless)	0.09
Power law x for exchange constant temperature	1.61
Curie temperature, T_C , of $\text{Fe}_{55}\text{Pt}_{45}$	$270 \text{ }^\circ\text{C}$
Curie temperature, T_C , of $\text{Fe}_{49}\text{Rh}_{51}$	$398 \text{ }^\circ\text{C}$

and the model then computes hysteresis loops at each temperature for which there are measured data. A global optimization is then performed, varying all unknown parameter values to minimize the sum of squares of the differences in coercivity between the model and experiment at each temperature:

$$\sum_{i=1}^N [H_c(T_i)_{\text{expt}} - H_c(T_i)_{\text{sim}}]^2 \quad (13)$$

At each step, the optimization of K_1 for $\text{Fe}_{49}\text{Rh}_{51}$ is recalculated using (10) and (11) because the exchange constant $C_2(T)$ is a free parameter in the optimization process. The resulting parameter values obtained from the minimization of the sum of squares in the unconstrained optimization are listed in Table I.

The model best-fit value of $K_1 = 1.77 \times 10^7 \text{ erg/cm}^3$ is within the expected bounds for thin films, which is typically less than the value of K_1 for bulk $\text{L1}_0 \text{ Fe}_{55}\text{Pt}_{45}$ of $6 \times 10^7 \text{ erg/cm}^3$ [30]. We also note this is consistent with the order parameter ($S = 0.55$) found from XRD measurements. The temperature dependence of K_1 in $\text{L1}_0 \text{ Fe}_{55}\text{Pt}_{45}$ is discussed by Richter and Parker [29], who determined an exponent for the anisotropy field of $x_H = 0.36$, which, taking Richter's assumed exponent for the saturation magnetization M_s of $x_M = 0.34$, gives an exponent for the anisotropy constant K_1 of $x_K = 0.7$. The model prediction of $x_K = 0.64$ is in reasonable agreement with the values obtained by Richter and Parker [29].

At $22 \text{ }^\circ\text{C}$, the model phenomenological exchange constant within the $\text{Fe}_{55}\text{Pt}_{45}$ layer, $C_1(0)$, calculated using the optimized parameter values and (12), has the value 0.113. The measured value of M_s for $\text{Fe}_{55}\text{Pt}_{45}$ is $= 1.16 \times 10^3 \text{ emu/cm}^3$ at $22 \text{ }^\circ\text{C}$. The optimized model exchange constant A for $\text{Fe}_{55}\text{Pt}_{45}$ is $2.9 \times 10^{-9} \text{ erg/cm}$ at $22 \text{ }^\circ\text{C}$. Theoretical and experimental values of A for 50-nm-thick films of $\text{Fe}_{48}\text{Pt}_{52}$ alloy are given in Ref. [31]

as 10.2 and $11.9 \pm 4 \times 10^{-9}$ erg/cm, respectively. The model optimized value of A for $\text{Fe}_{55}\text{Pt}_{45}$ is lower than that observed in Ref. [31], but this can be explained by the different thickness and deposition parameters of our films compared to [31]. To evaluate a model value for A for $\text{Fe}_{49}\text{Rh}_{51}$ at room temperature is more complex because the FM moment of $\text{Fe}_{49}\text{Rh}_{51}$ is minimal at 22°C . The peak value of M_s for $\text{Fe}_{49}\text{Rh}_{51}$ occurs at 120°C at which temperature $C_3(120)$ is 0.021 and $A = 0.233 \times 10^{-9}$ erg/cm.

The model best-fit exponent for the temperature dependence of the dimensionless exchange constant C , x_C is 1.61 , which is found from the relationship between A and C $x_A = x_C + 2x_M$. Using the optimized model result of $x_C = 1.61$ and our experimental fit value of $x_M = 0.396$, we obtain $x_A = 2.4$. The evolution of exchange coupling in $\text{Fe}_{49}\text{Rh}_{51}$ during the development of FM behavior is complex and the value of the exchange constant for $\text{Fe}_{49}\text{Rh}_{51}$ is unlikely to closely follow the behavior of (10).

Despite the relative simplicity of the layered macrospin model, it predicts the experimentally observed behavior of the samples very well. Figure 6 shows the simulated out-of-plane hysteresis loops for a range of temperatures from room temperature ($\text{RT} = 22^\circ\text{C}$) to 200°C . There is good agreement between Figs. 4 and 6 as far as the change in the form of the loops, coercivity, and saturation moment as a function of temperature.

The coercivity as a function of temperature determined from Fig. 6 is plotted alongside the experimental results in Fig. 5 where there is good agreement between simulated values and experiment results. We note that the simulation shows some small nonmonotonic behavior not present in the experimental data, which we ascribe to be due to the complexity of the evolution of the FM properties of $\text{Fe}_{49}\text{Rh}_{51}$ as a function of temperature, which is not fully represented by the layered macrospin model.

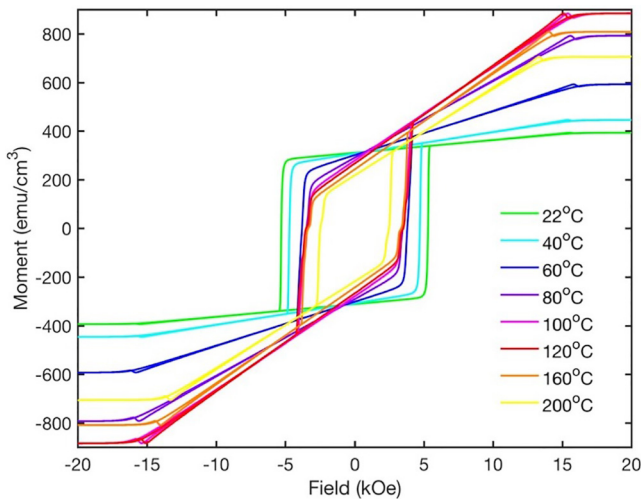


FIG. 6. Out-of-plane simulated hysteresis loops for the bilayer $\text{Fe}_{55}\text{Pt}_{45}/\text{Fe}_{49}\text{Rh}_{51}$ sample at a range of temperatures.

IV. PATTERNED MAGNETIC STRUCTURES

In order to understand whether or not the reduction in coercivity observed and modeled for continuous thin films remains as lateral dimensions are reduced, we determine the reversal behavior of meso-scale-patterned elements using the AHE. AHE offers the sensitivity required to observe the reversal of magnetic elements [19] where the small volume of material precludes standard magnetometry techniques. Since the characteristic AHE coefficient varies between materials and is highly temperature-dependent [32], it cannot be used to give a quantitative measure of M_s ; particularly in the case of $\text{Fe}_{49}\text{Rh}_{51}$, where the Hall resistivity of $\text{Fe}_{49}\text{Rh}_{51}$ is a complex function of temperature and applied field [33]. However, as the measured AHE voltage is proportional to the total perpendicular moment [33], it can be used to determine quantitative information on reversal processes as we have successfully demonstrated in previous work on the switching of magnetic nanostructures [34,35].

A circular magnetic island (diameter $1.7 \mu\text{m}$) is fabricated from the $\text{Fe}_{55}\text{Pt}_{45}/\text{Fe}_{49}\text{Rh}_{51}$ bilayer using electron-beam lithography, on to which a Pt Hall cross (arm width $2.5 \mu\text{m}$) is deposited to enable AHE measurements to be taken as a function of temperature, as shown in Fig. 7. Details of the island and Hall cross fabrication process are provided in the Appendix.

The sample is mounted in a chip carrier enabling the Hall cross to be wire-bonded for ease of connection to the measurement system. The AHE voltage is measured by applying an ac current of 0.8 mA at a frequency of 133 Hz (provided by a Keithley 6221 ac/dc current source) down one arm of the cross and the resulting transverse voltage is measured using a lock-in amplifier (Stanford Research Systems SR830) across the orthogonal arm of the cross [as illustrated in Fig. 7(a)]. The available maximum

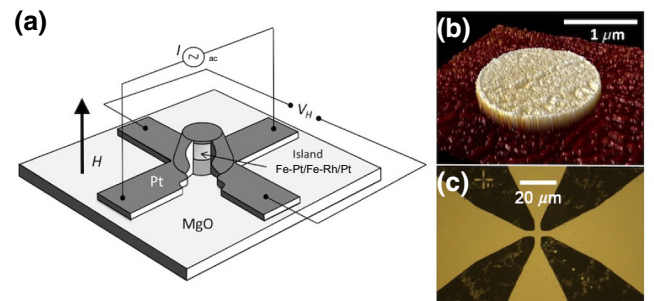


FIG. 7. (a) Pt Hall cross and AHE measurement geometry. The $\text{Fe}_{55}\text{Pt}_{45}/\text{Fe}_{49}\text{Rh}_{51}$ island is located under the center Pt Hall cross of width $2.5 \mu\text{m}$. AHE measurements are taken by applying an ac current, I , down one arm of the cross and the resulting Hall voltage, V_H , is measured across the adjacent arm as the applied field, H , is varied. (b) AFM image of the patterned island. (c) Optical microscope image of the Hall cross structure.

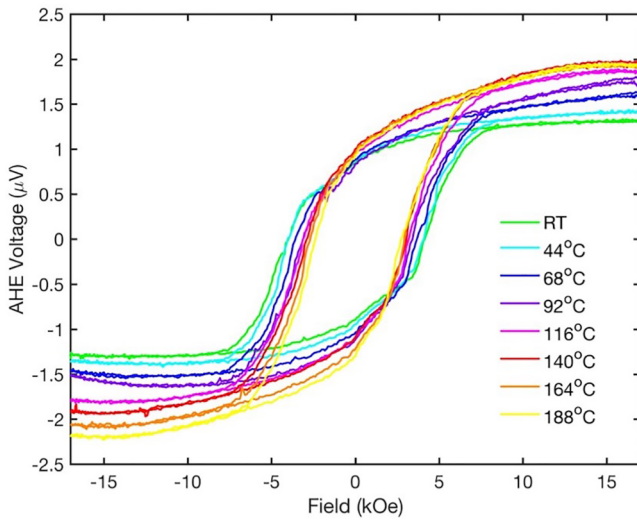


FIG. 8. Hysteresis loops for a 1.7- μm -diameter $\text{Fe}_{55}\text{Pt}_{45}/\text{Fe}_{49}\text{Rh}_{51}$ magnetic island measured at a range of temperatures using AHE.

magnetic field of 1.75 T is provided by a GMW Magnet Systems Model 3473-70 electromagnet and 231HC bipolar-current supply. When measuring each hysteresis loop, the out-of-plane magnetic field is swept at a rate of 300 Oe s^{-1} .

To enable temperature-dependent measurements, the mounted sample is placed inside a custom-built temperature-controlled heater mounted between the poles of an electromagnet. AHE is then used to produce hysteresis loops for the patterned structure as a function of temperature.

Figure 8 shows the measured hysteresis loops as a function of temperature for the $\text{Fe}_{55}\text{Pt}_{45}/\text{Fe}_{49}\text{Rh}_{51}$ island, where dc offsets and any linear contribution due to the ordinary Hall effect in the measured signal have been removed. The hysteresis loops show the essential features picked up by magnetometry measurements. However, the background contribution from the ordinary Hall effect at reduced geometries [33] is more complex, which accounts for the differences in the loop shape that cannot be easily corrected. As the coercivity is insensitive to any background subtraction, it can be directly compared with the magnetometry measurements of the bulk film.

The coercivity, H_c , as a function of temperature is extracted from the hysteresis loops measured using AHE and is plotted in Fig. 5 together with the data for the continuous film. A drop in H_c for the patterned structure is observed as the temperature is increased, which closely follows that of the continuous film indicating that any magnetic edge damage introduced by the ion-milling process has little effect on the switching of the structure at the island dimensions investigated [36]. These results indicate the value of the AHE technique for measuring the temperature-dependent switching of patterned

$\text{Fe}_{55}\text{Pt}_{45}/\text{Fe}_{49}\text{Rh}_{51}$ bilayer structures and demonstrating that patterning to these lateral dimensions maintains the exchange spring-mediated reversal process.

V. CONCLUSIONS

A bilayer thin film consisting of exchange-coupled $\text{Fe}_{55}\text{Pt}_{45}$ and $\text{Fe}_{49}\text{Rh}_{51}$ layers that exhibits a strong out-of-plane anisotropy is demonstrated. As the film is heated, a coercivity reduction is observed for modest temperature increases due to the $\text{Fe}_{49}\text{Rh}_{51}$ FM component assisting the switching of the high anisotropy $\text{Fe}_{55}\text{Pt}_{45}$ layer.

We present a simple, layered macrospin model that is used to simulate the switching of the $\text{Fe}_{55}\text{Pt}_{45}/\text{Fe}_{49}\text{Rh}_{51}$ bilayer system, which has been used to extract material parameters, including anisotropy and exchange constants. Although the model is relatively simple, and hence computationally cheap, it replicates the major features of the hysteresis loops at different temperatures well. We, therefore, conclude that it provides a reasonable description of the behavior of the bilayer using established Physics. This conclusion enables us to predict the behavior of similar bilayer systems with confidence.

The temperature-dependent switching behavior of an $\text{Fe}_{55}\text{Pt}_{45}/\text{Fe}_{49}\text{Rh}_{51}$ -patterned structure is investigated using AHE, which is shown to follow that of the continuous thin film, demonstrating that the temperature-assisted switching of the $\text{Fe}_{55}\text{Pt}_{45}$ is still observed after patterning.

This work provides a good foundation to optimize the structure and deposition conditions for $\text{Fe}_{55}\text{Pt}_{45}/\text{Fe}_{49}\text{Rh}_{51}$ thin films to achieve greater coercivity reduction and increased benefit from an exchange spring effect. AHE magnetometry is a powerful tool for analyzing structures patterned from such thin films and allows the impact of the interaction between the $\text{Fe}_{55}\text{Pt}_{45}$ and $\text{Fe}_{49}\text{Rh}_{51}$ layers to be further explored for future applications such as heat-assisted bit-patterned media.

ACKNOWLEDGMENTS

The authors would like to thank Rikagu Europe SE and Dr Tatjana Ulyanenkova for their help with the XRD measurements.

The authors gratefully acknowledge the support of the UK EPSRC through Grant No. EP/K008412/1. R. A. Griffiths acknowledges the North West Nanoscience Doctoral Training Centre (NOWNANO DTC) through Grant No. EP/G017905/1.

APPENDIX: FABRICATION METHODS

1. Thin film

The $\text{Fe}_{55}\text{Pt}_{45}(11)/\text{Fe}_{49}\text{Rh}_{51}(30)/\text{Pt}(2)$ (dimensions in nm, composition in at. %) thin film is deposited on to a $\text{MgO}(100)$ substrate using dc-magnetron sputtering in an AJA ATC2200 eleven target system. To improve the L_{10}

ordering of the Fe₅₅Pt₄₅ layer, an Fe-rich stoichiometry is chosen [22]. The base pressure before sputtering is less than 5×10^{-9} Torr and the Ar gas sputtering pressure during deposition is 3×10^{-3} Torr. In order to minimize the dewetting effects, 2 nm of Fe₅₅Pt₄₅ is initially sputtered and then baked at 650 °C for 2 h. The remaining 9 nm of Fe₅₅Pt₄₅ is deposited and then further annealed at 750 °C for 2 h to form the L1₀ phase. Following this, the temperature is reduced to 500 °C and the Fe₄₉Rh₅₁ layer is deposited. The sample is allowed to cool for 4 h after which a 2-nm Pt cold-capping layer is deposited.

2. Patterned islands and Hall cross

To fabricate the circular island in the fabricated Fe₅₅Pt₄₅/Fe₄₉Rh₅₁ thin film, a hard mask for ion milling is formed by spinning a thick negative-electron-beam resist layer (MicroChem ma-N2403), which is exposed using a Zeiss EVO electron-beam lithography system at a dose of 200 $\mu\text{C cm}^{-2}$. Following development using Shipley Microposit MF-26A developer, a resist pillar is left on top of the film surface. Next, any unprotected film is removed by ion milling, using Ar⁺ ions at 2 kV, 17.8 mA, following which any remaining resist is removed using Shipley Microposit 1165 remover to leave a Fe₅₅Pt₄₅/Fe₄₉Rh₅₁ magnetic island on the MgO substrate. In previous work [34,35], we have used the thin-film seed layer to form the Hall cross to enable AHE measurements to be performed. However, as there is no metal seed layer present in this bilayer film structure, the Hall cross is formed by depositing a Pt cross structure over the island as illustrated in Fig. 7. The Hall cross structure is produced using lift-off following a second optical lithography step. A thick positive bilayer resist consisting of a MicroChem Polymethylglutarimide (PMGI) resist layer followed by a Shipley Microposit S1805 resist layer is spun onto the substrate. The cross structure is defined in the resist layer by optical lithography using a Microtech LW405 laser writer such that the Fe₅₅Pt₄₅/Fe₄₉Rh₅₁ island is located in the center of a cross. Following development in MicroChem MF319 developer, a cross shape is produced in the resist layer on to which a 30-nm layer of Pt is sputtered using the AJA ATC-2200 system. Using lift-off, any remaining resist is removed using 1165 remover to leave a Pt Hall cross on top of the magnetic island. The width of each Hall cross arm is 2.5 μm .

-
- [1] M. Jiang, X. Z. Chen, X. J. Zhou, Y. Y. Wang, F. Pan, and C. Song, Influence of film composition on the transition temperature of FeRh films, *J. Cryst. Growth* **438**, 19 (2016).
 [2] O. Kubaschewski, *IRON – Binary Phase Diagrams* (Springer-Verlag, West Berlin, 1982).
 [3] M. Fallot, Less Alliages Du Fer Avec Les Métaux De La Famille Du Platine, *Ann. Phys. (N.Y.)* **10**, 291 (1938).

- [4] J. S. Kouvel and C. C. Hartelius, Anomalous magnetic moments and transformations in ordered alloy FeRh, *J. Appl. Phys.* **33**, 1343 (1962).
 [5] D. Weller, O. Mosendz, G. Parker, S. Pisana, and T. S. Santos, L1₀ FePtX–Y media for heat-assisted magnetic recording, *Phys. Status Solidi A* **210**, 1245 (2013).
 [6] M. H. Kryder, E. C. Gage, T. W. McDaniel, W. A. Challener, R. E. Rottmayer, G. Ju, Y.-T. Hsia, and M. F. Erden, Heat assisted magnetic recording, *Proc. IEEE* **96**, 1810 (2008).
 [7] D. Weller, G. Parker, O. Mosendz, E. Champion, B. Stipe, X. Wang, T. Klemmer, G. Ju, and A. Ajan, A HAMR technology roadmap to an areal density of 4 Tb/in², *IEEE Trans. Magn.* **50**, 3100108 (2014).
 [8] G. Ju, Y. Peng, E. K. C. Chang, Y. Ding, A. Q. Wu, X. Zhu, Y. Kubota, T. J. Klemmer, H. Amini, L. Gao, Z. Fan, T. Rausch, P. Subedi, M. Ma, S. Kalarickal, C. J. Rea, D. V. Dimitrov, P.-W. Huang, K. Wang, X. Chen, C. Peng, W. Chen, J. W. Dykes, M. A. Siegler, E. C. Gage, R. Chantrell, and J.-U. Thiele, High density heat-assisted magnetic recording media and advanced characterization – Progress and challenges, *IEEE Trans. Magn.* **51**, 3201709 (2015).
 [9] X. Z. Chen, J. F. Feng, Z. C. Wang, J. Zhang, X. Y. Zhong, C. Song, L. Jin, B. Zhang, F. Li, M. Jiang, Y. Z. Tan, X. J. Zhou, G. Y. Shi, X. F. Zhou, X. D. Han, S. C. Mao, Y. H. Chen, X. F. Han, and F. Pan, Tunneling anisotropic magnetoresistance driven by magnetic phase transition, *Nat. Commun.* **8**, 449 (2017).
 [10] R. O. Cherifi, V. Ivanovskaya, L. C. Phillips, A. Zobelli, I. C. Infante, E. Jacquet, V. Garcia, S. Fusil, P. R. Briddon, N. Guiblin, A. Mougin, A. A. Ünal, F. Kronast, S. Valencia, B. Dkhil, A. Barthélémy, and M. Bibes, Electric-field control of magnetic order above room temperature, *Nat. Mater.* **13**, 345 (2014).
 [11] X. Marti, I. Fina, C. Frontera, J. Liu, P. Wadley, Q. He, R. J. Paull, J. D. Clarkson, J. Kudrnovský, I. Turek, J. Kunes, D. Yi, J.-H. Chu, C. T. Nelson, L. You, E. Arenholz, S. Salahuddin, J. Fontcuberta, T. Jungwirth, and R. Ramesh, Room-temperature antiferromagnetic memory resistor, *Nat. Mater.* **13**, 367 (2014).
 [12] A. M. Tishin and Y. I. Spichkin, Recent progress in magnetocaloric effect: Mechanisms and potential applications, *Int. J. Refrig.* **37**, 223 (2014).
 [13] J.-U. Thiele, S. Maat, and E. E. Fullerton, FeRh/FePt exchange spring films for thermally assisted magnetic recording media, *Appl. Phys. Lett.* **82**, 2859 (2003).
 [14] J.-U. Thiele, S. Maat, J. L. Robertson, and E. E. Fullerton, Magnetic and structural properties of FePt–FeRh exchange spring films for thermally assisted magnetic recording media, *IEEE Trans. Magn.* **40**, 2537 (2004).
 [15] K. Y. Guslienko, O. Chubykalo-Fesenko, O. Mryasov, R. Chantrell, and D. Weller, Magnetization reversal via perpendicular exchange spring in FePt/FeRh bilayer films, *Phys. Rev. B* **70**, 104405 (2004).
 [16] H. Kronmüller and D. Goll, Micromagnetic theory of the pinning of domain walls at phase boundaries, *Physica B* **319**, 122 (2002).
 [17] C. Vogler, C. Albert, F. Bruckner, D. Suess, and D. Praetorius, Heat-assisted magnetic recording of bit-patterned media beyond 10 Tb/in², *Appl. Phys. Lett.* **108**, 102406 (2016).

- [18] Y. Wang and B. V. K. Vijaya Kumar, Write modeling and read signal processing for heat-assisted bit-patterned media recording, *IEEE Trans. Magn.* **54**, 3000510 (2018).
- [19] A. Neumann, C. Thönnißen, A. Frauen, S. Heße, A. Meyer, and H. Peter, Probing the magnetic behavior of single nanodots, *Nanoletters* **13**, 2199 (2013).
- [20] S. D. Granz and M. H. Kryder, Granular L1₀ (001) thin films for heat assisted magnetic recording, *J. Magn. Magn. Mater.* **324**, 287 (2012).
- [21] S. D. Granz, K. Barmak, and M. H. Kryder, Granular L1₀ FePt:X (X = Ag, B, C, SiO_x, TaO_x) thin films for heat assisted magnetic recording, *Eur. Phys. J. B* **86**, 81 (2013).
- [22] J.-U. Thiele, M. Buess, and C. H. Back, Spin dynamics of the antiferromagnetic-to-ferromagnetic phase transition of FeRh on a sub-picosecond time scale, *Appl. Phys. Lett.* **85**, 2857 (2004).
- [23] T. Ono, H. Nakata, T. Moriya, N. Kikuchi, S. Okamoto, O. Kitakami, and T. Shimatsu, Addition of Ru to L1₀-FePt thin film to lower Curie temperature, *Appl. Phys. Expr.* **9**, 123002 (2016).
- [24] C. W. Barton, T. A. Ostler, D. Huskisson, C. J. Kinane, S. J. Haigh, G. Hrkac, and T. Thomson, Substrate induced strain filed in FeRh epilayers grown on single crystal MgO (001) substrates, *Sci. Rep.* **7**, 44397 (2017).
- [25] C. Kittel, *Introduction to Solid State Physics*, 8th ed. (Wiley, New York, 2004), ISBN: 978-0-471-41526-8.
- [26] D. Weller, A. Moser, L. Folks, M. E. Best, W. Lee, M. F. Toney, M. Schwicket, J.-U. Thiele, and M. F. Doerner, High K_u materials approach to 100 Gbits/in², *IEEE Trans. Magn.* **36**, 10 (2000).
- [27] T. Bublath and D. Goll, Temperature dependence of the magnetic properties of L1₀-FePt nanostructures and films, *J. Appl. Phys.* **108**, 113910 (2010).
- [28] R. F. L. Evans, W. J. Pan, P. Chureemart, T. A. Ostler, M. O. A. Ellis, and R. W. Chantrell, Atomistic spin model simulations of magnetic nanomaterials, *J. Phys.: Condens. Matter* **26**, 103202 (2014).
- [29] H. J. Richter and G.J. Parker, Temperature Dependence of the Anisotropy Field of L10 FePt near the Curie Temperature, arXiv:1703.10921 [cond-mat.mes-hall].
- [30] K. H. J. Buschow, *Handbook of Magnetic Materials*, Volume 19, 1st Ed (Elsevier, Amsterdam, 2010), ISBN: 978-0-444-53780-5.
- [31] C. Antoniak, J. Lindner, K. Fauth, J.-U. Thiele, J. Minár, S. Mankovsky, H. Ebert, H. Wende, and M. Farle, Composition dependence of exchange stiffness in Fe_xPt_{1-x} alloys, *Phys. Rev. B* **82**, 064403 (2010).
- [32] E. M. Pugh and N. Rostoker, Hall effect in ferromagnetic materials, *Rev. Mod. Phys.* **25**, 151 (1952).
- [33] M. A. de Vries, M. Loving, A. P. Mihai, L. H. Lewis, D. Heiman, and C. H. Marrows, Hall-effect characterization of the metamagnetic transition in FeRh, *New J. Phys.* **15**, 013008 (2013).
- [34] M. Alexandrou, P. W. Nutter, M. Delalande, J. de Vries, E. W. Hill, F. Schedin, L. Abelmann, and T. Thomson, Spatial sensitivity mapping of Hall crosses using patterned magnetic nanostructures, *J. Appl. Phys.* **108**, 043920 (2010).
- [35] R. A. Griffiths, P. W. Nutter, A. Neumann, C. Thönnißen, E.-S. Wilhelm, and T. Thomson, Signal asymmetries in the anomalous Hall effect of bilayer magnetic nanostructures, *Appl. Phys. Lett.* **109**, 132401 (2016).
- [36] J. M. Shaw, S. E. Russek, T. Thomson, M. J. Donahue, B. D. Terris, O. Hellwig, E. Dobisz, and M. L. Schneider, Reversal mechanisms in perpendicularly magnetized nanostructures, *Phys. Rev. B* **78**, 024412 (2008).